Moisture determination of concrete panel using SAR imaging and the K-R-I transform
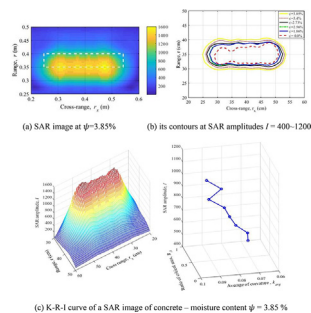
Ahmed Alzeyadi, Tzuyang Yu *

Department of Civil and Environmental Engineering, University of Massachusetts Lowell, One University Avenue, Lowell, MA 01854, USA

HIGHLIGHTS

- Preparing concrete specimens at different levels of moisture content.
- Imaging concrete specimens with synthetic aperture radar using microwave.
- Tests include air-drying and oven heating of Portland cement concrete specimen.
- Analyzing radar images to extract local and global features for subsurface moisture determination in concrete.
- Developing quantitative models from radar images for predicting moisture content inside concrete.

GRAPHICAL ABSTRACT

(a) SAR image at ψ=3.85%   (b) its contours at SAR amplitudes *I* = 400–1200

(c) K-R-I curve of a SAR image of concrete – moisture content ψ = 3.85 %

ARTICLE INFO

ABSTRACT

Moisture content inside concrete affects the properties and behaviors of Portland cement concrete. It also indicates the likelihood of structural damages (e.g., steel corrosion) in reinforced and prestressed concrete structures. While several laboratory techniques are available for moisture determination, it is a challenging task to estimate the moisture content of concrete in the field without using embedded moisture sensors. In this paper, synthetic aperture radar (SAR) imaging and the K-R-I (curvature-area-amplitude) transform were applied to a concrete panel specimen (water-to-cement ratio = 0.45) for moisture determination. A 10.5 GHz center frequency radar system was used to generate SAR images of the concrete panel at various moisture levels from 0% to 3.85% (by mass). Quantitative analysis of SAR images was carried out by the K-R-I transform to understand the simultaneous change of SAR amplitude and shape at different moisture levels. It was found that integrated SAR amplitude and average maximum SAR amplitude both increase nonlinearly with the increase of moisture content in the concrete panel. Spatial distribution of SAR amplitudes can be used to indicate subsurface moisture distribution in concrete. The area-amplitude (R-I) curve of SAR images quantifies the relationship between moisture content and its distribution.

1. Introduction

Moisture content inside Portland cement concrete is instrumental to predicting the short-term strength development (cement hydration) and long-term durability performance of concrete (reinforced and prestressed) structures, as well as to detecting

* Corresponding author.
E-mail addresses: Ahmed_AlZeyadi@student.uml.edu (A. Alzeyadi), Tzuyang_yu @uml.edu (T. Yu).

structural damages such as steel corrosion inside concrete. Not only does moisture inside concrete facilitate most durability problems (e.g., freezing-and-thawing [1–3,7], steel corrosion [4], carbonation [5], alkali-silica reaction (ASR) [6] in concrete structures, its amount and distribution also indicate the hydraulic permeability of concrete. In the freeze-thaw damage of non-air-entrained concrete, it has been reported that concrete will experience significant damage when its moisture content exceeds 80% [9]. In the chloride-induced corrosion of steel rebar inside concrete structures, high moisture content promotes the diffusion of water molecules through the capillary pores inside concrete [4,8]. Carbonation of concrete can be encouraged when the relative humidity inside concrete is between 55% and 65% [8]. Research has also shown that expansive ASR can occur in concrete when relative humidity is above 80% [9]. In addition, it is well known that saturated concrete is weaker than dry concrete by approximately 20% [10,11].

Knowing that moisture content in concrete is crucial to the performance of concrete structures, it is, however, difficult to determine the moisture content inside concrete in the field without using intrusive or embedded moisture sensors. To avoid troublesome issues associated with embedded moisture sensors, nondestructive testing/evaluation (NDT/E) techniques can be applied. Among existing NDT/E techniques, gravimetric technique [12,13], gammadensitometry technique [14,15] moisture sensors [16] thermal and microwave/radar methods [17,18] have been applied for moisture determination. The gravimetric technique is destructive and not applicable for field structures. The gammadensitometry technique is radioactive and requires coordinated inspection of a transmitting source and a receiving collimator, making it very difficult for field implementation. Commercial moisture sensors are intrusive and need to be embedded inside concrete as an anomaly. They cannot be applied to existing structures. In general, an ideal NDT/E technique for moisture determination in concrete must be quantitative, capable of detecting internal moisture distribution, and invulnerable to environmental factors (e.g., temperature, soluble salt content [19]. Ultimately, such technique should be capable of quantifying different phases (free water, bound water, and chemically bound water) of moisture inside concrete [20].

Electromagnetic techniques such as ground penetrating radar (GPR) are capable of conducting spatial and semi-quantitative moisture determination in concrete specimens [17,18,21,22] and structures [11,23]. Since electromagnetic waves (radar signals) are capable of penetrating through dielectrics like concrete, they are inherently applicable for subsurface sensing problems in concrete. Laurens et al. [24] used a 1.5 GHz center frequency GPR system to evaluate the moisture content of 0.25x0.25x0.07 m concrete slabs at various saturation levels (0–100%). They found that GPR signal attenuates linearly with the increase of moisture content. They also reported that the presence of moisture reduces the center frequency of reflected GPR signal in another similar study [17] studied the amplitudes of direct and reflected GPR signals with a center frequency of 1.5 GHz inside concrete slabs (0.75 × 0.5 × 0.08 m) at different moisture levels (0, 20, 40, 60, 80 and 100%). They found that amplitudes of direct and reflected GPR signals decrease linearly with the increase of moisture content. Klysz and Balayssac [25] applied a GPR (SIR-2000 radar system, equipped with two 1.5 GHz coupled antenna (5100)) system on concrete slabs (0.6 × 0.6 × 0.12 m) with various moisture contents (0–15.3% by volume) to investigate the effect of moisture on GPR signal amplitude and signal velocity. They found that both amplitude and velocity of the GPR signal reduce with the increase in moisture content (as an indication of dielectric dispersion). In addition, while most researchers reported linear attenuation of GPR signals with the increase of moisture content in concrete, some reported a nonlinear attenuation between GPR signal and moisture content [26,27].

From the literature review, it was reported that the amplitude of direct and reflected GPR signal from concrete specimens decreases with the increase of moisture content inside concrete. This relationship was characterized by linear models in most reported results. Other imaging radar techniques (besides GPR) have not been reported for moisture determination in concrete.

The objective of this paper is to apply synthetic aperture radar (SAR) imaging for moisture determination of a concrete panel specimen. SAR imaging is a relatively new technique in civil engineering applications. Compared to GPR, SAR imaging utilizes image superposition to improve resolution and damage detectability. In this research, a laboratory 10.5 GHz center frequency radar system was used to generate SAR images of the concrete panel. The concrete panel was air dried in a temperature-controlled room condition for 30 days to achieve up to 3.85% of moisture variation. In this paper, principle of SAR imaging is briefly introduced, followed by experimental work on specimen preparation, moisture monitoring, and laboratory SAR imaging. Finally, research findings are summarized and concluded.

2. Principle of SAR imaging

In synthetic aperture radar (SAR) imaging, high-resolution coherent (continuous wave) images are produced with adjustable frequency bandwidth and artificial radar aperture. Not only higher frequencies and wider bandwidths can lead to high-resolution SAR images, increased radar aperture created by prolonged radar movement can also produce SAR images with better resolution. Producing such coherent images from raw SAR data is essentially an image formation process. In SAR imaging, back-scattering pattern of any target is first formulated by a planar scattering problem in a domain Ω_s containing N scattering points (Fig. 1). In Fig. 1, θ_i is the incident angle and θ_s the reflection/scattered angle.

Consider an incident electromagnetic (EM) wave with unit amplitude as follows [28].

$$\psi_{\text{inc}}(\bar{r}) = \frac{1}{r}.\exp(i\bar{k}_i.\bar{r}). \tag{1}$$

where $\bar{k}_i = k_{ix}\hat{x} - k_{iy}\hat{y}$ = incident wave vector, $\bar{r}$ = position vector from the radar to any observation point ($|\bar{r}| = r$), k_{ix}, k_{iy} = wave number components in x and y axes. The scattered field from scatterer j located at $\bar{r}_j$ and observed at $\bar{r}$ can be determined by [29].

$$\psi_{\text{scat}}(\bar{r}, \bar{r}_j) = \frac{s_j(\bar{r}, \hat{k}_i)}{|\bar{r} - \bar{r}_j|} \cdot \exp(ik|\bar{r} - \bar{r}_j|) \cdot \psi_{\text{inc}}(\bar{r}) \tag{2}$$

where $s_j = s_j(\bar{r}, \hat{k}_i)$ = scattered amplitude at scatterer j due to an incident wave at $\hat{k}_i$ and observed at $\bar{r}$, $i = \sqrt{-1}$ as the imaginary
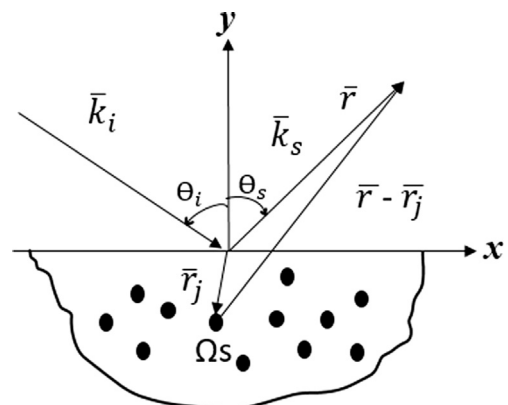

Fig. 1. Scattering of a domain with N scattering points.

number, $k = \omega/c$ as the wave number, ω = incident frequency, and $c \cong 2.998 \times 10^8$ = speed of EM waves ($c \cong 2.998 \times 10^8$ m/s in free space). Should we neglect the higher order scattering (scattered fields due to multiple reflections) among scatterers in this formulation, the total scattered field from N scatterers observed at $\bar{r}$ is the summation of all the scattered fields as

$$\psi_{\text{scat}}(\bar{r}) = \sum_{j=1}^{N} \frac{s_j(\bar{r}, \hat{k}_i)}{|\bar{r} - \bar{r}_j|} \cdot \exp(ik|\bar{r} - \bar{r}_j|) \cdot \psi_{\text{inc}}(\bar{r}) \qquad (3)$$

where $\bar{k}_s = k_{sx}\hat{x} + k_{sy}\hat{y}$ = scattering direction vector, and $\bar{k}_s = -\bar{k}_i$ when the radar operates in monostatic mode. Considering the case of a single scatterer without losing generality, Eq. (3) can be written as

$$\psi_{\text{scat}}(\omega, \theta) = \psi_{\text{scat}}(k, \bar{r}_s) = \frac{s_\theta}{r^2}.\exp\left[i\frac{r}{c}\omega(1 + \cos^2\theta - \sin^2\theta)\right] \qquad (4)$$

where $\theta = \theta_i = \tan^{-1}(k_{iy}/k_{ix})$. Eq. (4) is obtained by taking a slice of the two-dimensional (2-D) Fourier transform (FT) of domain Ω_s. In backprojection algorithms, 1-D IFT is first performed to generate sub-images, following by image superposition to result in a final SAR image. A frequency modulation operator (or time-domain convolution operator) is applied to ensure that the center in backprojection images coincides with the center of the target. A frequency domain shifting-back step is carried out in backprojection algorithms by applying a ramp filter in which frequency ω_n is shifted back by a carrier frequency ω_c.

$$\begin{aligned}
P(v, \theta) &= \int_{\omega_{\min}}^{\omega_{\max}} d\omega.\psi_{\text{scat}}(\omega - \omega_c, \theta)|\omega - \omega_c|.\exp(-i\omega v) \\
&= \frac{s_\theta}{r^2} \cdot \int_{\omega_{\min}}^{\omega_{\max}} d\omega.|\omega \\
&\quad - \omega_c|.\exp\left[i\frac{r}{c}(\omega - \omega_c) \times (1 + \cos^2\theta - \sin^2\theta) - i\omega v\right]
\end{aligned} \qquad (5)$$

where v = spatial variable of the 1-D IFT projection. Translating local 1-D IFT coordinates $[v, P(v, \theta_s)]$ to global polar coordinates (r, ϕ) indicates that

$$v = r\cos(\phi - \theta_s) \qquad (6)$$

In this coordinate transformation, upsampling is commonly required to ensure the quality of backprojection images. In other words, $P[r\cos(\phi - \theta), \theta]$ is obtained by interpolating $P(v, \theta)$. In the polar coordinate system, a backprojection image is finally obtained by integrating sub-images at various azimuth angles over the entire inspection range (synthetic aperture).

$$\begin{aligned}
I(r, \phi) &= \int_{-\theta_{\text{int}/2}}^{\theta_{\text{int}/2}} d\theta.P(r\cos(\phi - \theta), \theta) \\
&= \frac{s_\theta}{r^2} \cdot \int_{-\theta_{\text{int}/2}}^{\theta_{\text{int}/2}} d\theta \int_{\omega_{\min}}^{\omega_{\max}} d\omega.|\omega \\
&\quad - \omega_c|.\exp\left[i\frac{r}{c}(\omega - \omega_c)(1 + \cos^2\theta - \sin^2\theta) - i\omega r\cos(\phi - \theta_s)\right].
\end{aligned} \qquad (7)$$

where the polar coordinates (r, ϕ) are related to the Cartesian coordinates (x, y) by

$$x = r\cos\phi. \qquad (8)$$

$$y = r\sin\phi. \qquad (9)$$

By doing so, the image plane $I(x, y) = I(r\cos\phi, r\sin\phi)$ can be reconstructed. Fig. 2 illustrates the key processing step of the backprojection algorithm adopted in this research.
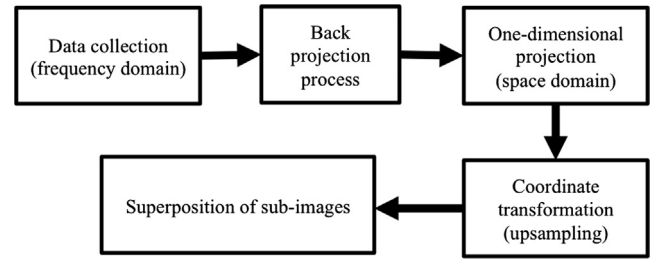

Fig. 2. Backprojection algorithm processing steps.

3. Experimental work

3.1. Specimen preparation

A concrete panel specimen ($0.3 \times 0.3 \times 0.05$ m) was manufactured for characterizing moisture variation in concrete. Type I/II Portland cement was used. The mix design ratio of concrete panel was 0.45:1:2:4 (by weight) for water: cement: sand: aggregate. The concrete panel was moist cured for 28 days before it was left in a room condition environment (temperature = 25.8 ± 1.07 °C, relative humidity = $16.5 \pm 6.08\%$) for air-drying. After approximately five months of air-drying, the concrete panel was oven heated at 80 °C for thirty days. Table 1 shows the mix design proportions of concrete. Fig. 3 provides a picture of the concrete panel and its dimensions.

3.2. Moisture monitoring

In this research, change of moisture content in concrete over time was measured by monitoring the mass of concrete panel at different stages of air-drying. An electronic scale (Model: V11P15 by Ohaus Corp.) with ± 1 gm accuracy was used for measuring the mass of concrete panel for approximately five months. The moisture content of concrete panel was calculated by the following equation.

$$\psi(t) = \left[\frac{m_w(t) - m_d}{m_d}\right] \cdot 100\% \qquad (10)$$

where $\psi(t)$ = moisture content at time t (%), $m_w(t)$ = mass of concrete panel at a given air-drying time t (g), and m_d = oven-heated mass of concrete panel (g). The concrete panel was oven-heated at 80 °C for thirty days until the mas stabilized in the end of the moisture measuring period. An electronic oven (Model: BLUE M by Electric Company) in Geotechnical Laboratory in Department of Civil and Environmental Engineering at UMass Lowell was used to produce the oven-heated concrete panel. The reason for choosing a relatively low temperature (80 °C) was to avoid concrete cracking due to excessive internal thermal stress. The oven-heated mass m_d was assumed to be the zero-moisture mass of concrete, for only capillary and pore water was considered for moisture determination in this research.

3.3. Synthetic aperture radar imaging

Synthetic aperture radar (SAR) imaging of the concrete panel at different moisture contents was performed by using a 10.5 GHz center frequency continuous wave imaging radar (CWIR) system

Table 1
Mix design of concrete.

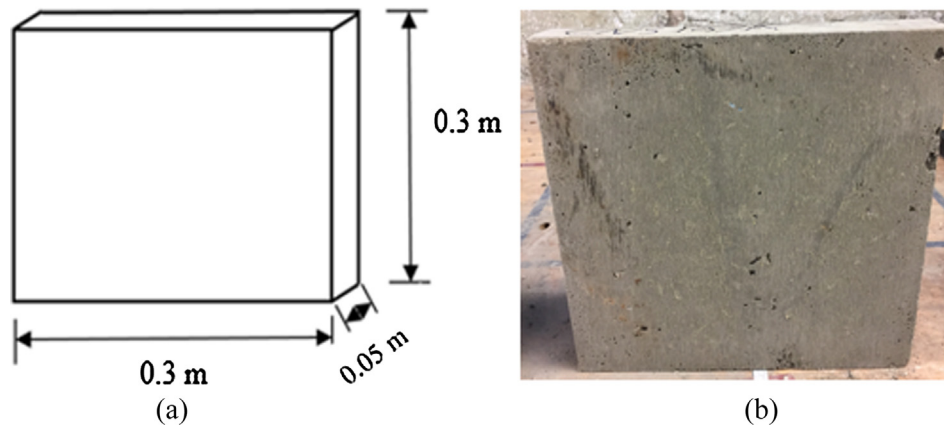| Cement (kg/m³)	Sand (kg/m³)	Aggregate (kg/m³)	Water (kg/m³)
300	600	1200	135

Fig. 3. Schematic (a) and picture (b) of concrete panel.

with a 1.5 GHz bandwidth. Stripmap SAR imaging mode was adopted, and all SAR images were collected inside an anechoic chamber in Electromagnetic Remote Sensing Laboratory (ERSL) at UMass Lowell. The use of an anechoic chamber would allow us to develop noise-free SAR images for data analysis and modeling. The CWIR system moved along the cross-range axis for 0.8 m to cover the entire concrete panel at a constant range of 0.35 m for all SAR images. Fig. 4 shows the experimental configuration of SAR imaging.

4. Results and findings

4.1. Effect of moisture content on 2-D SAR images of concrete

SAR images of the concrete panel specimen developed at different times of air-drying to create various moisture contents are shown in Fig. 5. These SAR images are rendered in a 2-D range vs. cross-range (r, r_x) domain. In each SAR image, EM scattering responses (at different locations on a synthetic aperture) from a target are processed and integrated by the backprojection algorithm. The integrated EM scattering response is rendered by 2-D SAR amplitudes in an SAR image. The physical meaning of SAR amplitudes is related to the dielectric properties (dielectric constant and loss factor, or relative complex electric permittivity) of a target. The real part of relative complex electric permittivity (or dielectric constant) indicates the dielectric amplification (energy storage) of a target, while the imaginary part (or loss factor) relates to the dielectric attenuation (energy dissipation) of a target. When the moisture content of concrete increases, the effective dielectric

constant of wet concrete is expected to increase from the one of dry concrete. This is because the dielectric constant of moisture or liquid water has a dielectric constant of 78–81 in the microwave frequency range (300 MHz–300 GHz), and the dielectric constant of dry concrete generally ranges from 4 (lightweight concrete) to 15 (heavyweight concrete) in the microwave frequency range. Therefore, theoretically speaking, the increase of moisture content is expected to result in the increase of SAR amplitudes.

In Fig. 5, it was experimentally confirmed that the increase of moisture content leads to the increase of SAR amplitudes. Comparing Fig. 5(a) (3.85% moisture content) and (e) (0% moisture content), the warmer colors correspond to greater SAR amplitudes, suggesting stronger EM scattering responses. Furthermore, the distribution of SAR amplitudes in Fig. 5 also expands from 0% moisture content (Fig. 5(e)) to 3.85% moisture content (Fig. 5(a)). This experimental observation not only confirms the validity of subsurface sensing in concrete using EM waves, but also indicates the feasibility of using SAR images for subsurface moisture mapping.

To better quantify the relationship between SAR amplitude and moisture content, two parameters derived from SAR images were used; integrated SAR amplitude I_{int} and average SAR amplitude I_{avg}. Integrated SAR amplitude of an SAR image is defined by

$$I_{int} = \int \int I(r, r_x) dr dr_x \tag{11}$$

while average SAR amplitude of an SAR image is defined by

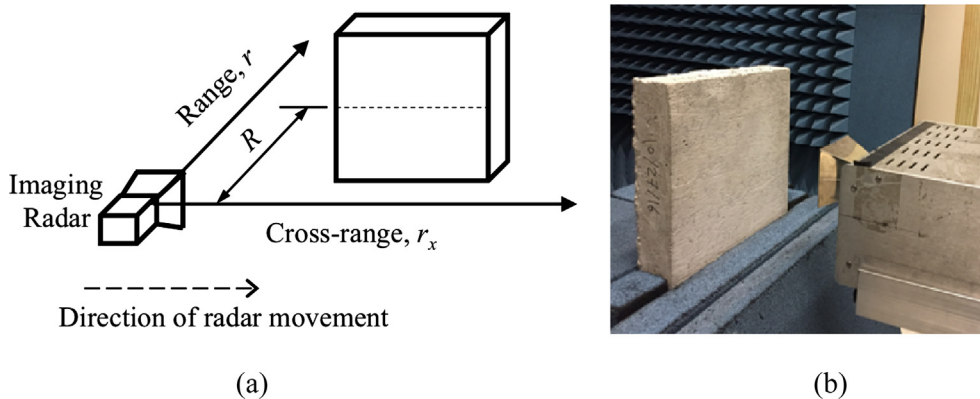$$I_{avg} = \frac{1}{n} \sum_{j=1}^{n} \max_j I(r, (r_x)_j) \tag{12}$$

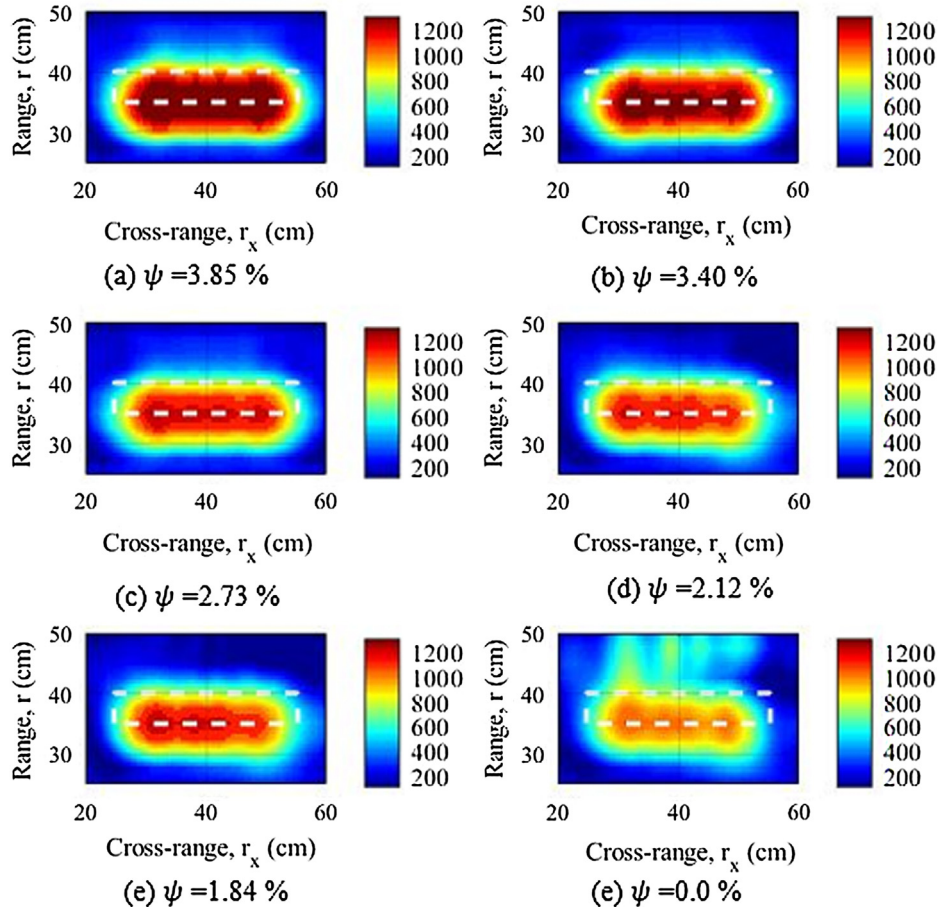**Fig. 4.** Schematics (a) and picture (b) of SAR imaging system.

Fig. 5. SAR images of concrete panel at different moisture contents (ψ = moisture content).
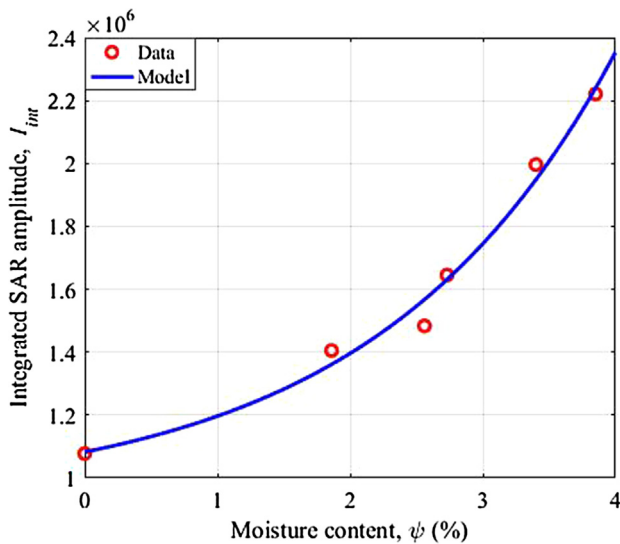

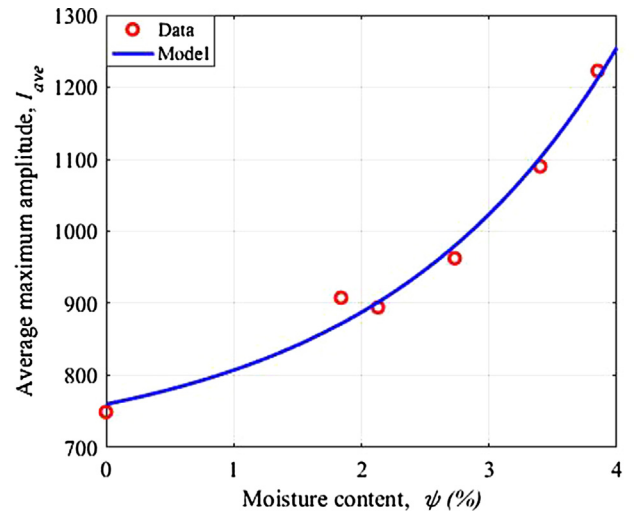**Fig. 6.** Integrated SAR amplitude vs. moisture content.

Fig. 7. Average maximum SAR amplitude vs. moisture content.

where n = number of cross-range values for averaging local maximum SAR amplitudes. With Eqs. (11) and (12), I_{int} and I_{avg} values of SAR images of concrete with different moisture contents were calculated as shown in Figs. 6 and 7.

In Figs. 6 and 7, it was found that the increase of moisture content of concrete leads to a nonlinear increase of both I_{int} and I_{avg}.

Consequently, predictive models were developed from Figs. 6 and 7, as shown in the following.

$$I_{int}(\psi) = a_1 e^{b_1 \psi} + c_1 \tag{13}$$

where $I_{int}(\psi)$ = integrated SAR amplitude with moisture content ψ, ψ = moisture content (%), a_1, b_1, and c_1 = model constants

$(a_1 = 1.525e5, b_1 = 0.5585, c_1 = 9.303e5)$. The R^2 value of the model in Fig. 6 was 0.986.

$$I_{avg}(\psi) = a_2 e^{b_2 \psi} + c_2 \tag{14}$$

where $I_{avg}(\psi)$ = average maximum SAR amplitude with moisture content ψ, a_2, b_2, and c_2 = constants ($a_2 = 67.85$, $b_2 = 0.5289$, $c_2 = 692.3$). The R^2 value of the model in Fig. 7 was 0.985. Since our objective was to determine moisture content ψ, Eqs. (13) and (14) were converted into Eqs. (15) and (16), respectively.

$$\psi_{est}(I_{int}) = \frac{1}{b_1} \log \left[\frac{I_{int} - c_1}{a_1} \right] \tag{15}$$

$$\psi_{est}(I_{avg}) = \frac{1}{b_2} \log \left[\frac{I_{avg} - c_2}{a_2} \right] \tag{16}$$

where $\psi_{est}(I_{int})$ = estimated moisture content (%) using integrated SAR amplitude I_{int}, and $\psi(I_{avg})$ = estimated moisture content (%) using average maximum SAR amplitude I_{avg}. Eqs. (15) and (16) represent two models for estimating moisture content inside a concrete panel.

4.2. Effect of moisture content on subsurface SAR amplitudes

Since the nature of 2-D SAR images enables researchers to explore the subsurface condition of a target, it is important to know how SAR amplitudes attenuate in the subsurface region of a target. To achieve the goal, 1-D SAR curves were extracted from the SAR images in this paper for better analysis. Figs. 8 and 9 provide two examples of extracting 1-D SAR curves from their 2-D images.

In Fig. 8(b), the maximum SAR amplitude (the first peak) indicates the backprojected location of the front side of concrete panel at $\psi = 0\%$ moisture content. This maximum SAR amplitude locates at 35 cm range. A second peak is found at 47.5 cm range, indicating the subsurface reflection from the backside of concrete panel.

When moisture content was increased from $\psi = 0\%$ to $\psi = 3.85\%$, the second peak disappeared (Fig. 9(b). This result was expected because the presence of moisture not only can enhance the dielectric significance (real part or dielectric constant) but also can amplify the dielectric attenuation (imaginary part or loss factor) of concrete (wet concrete is more lossy or conductive than dry concrete). As a result, no subsurface SAR amplitude representing the backside reflection can be found in Fig. 9(b), due to signal
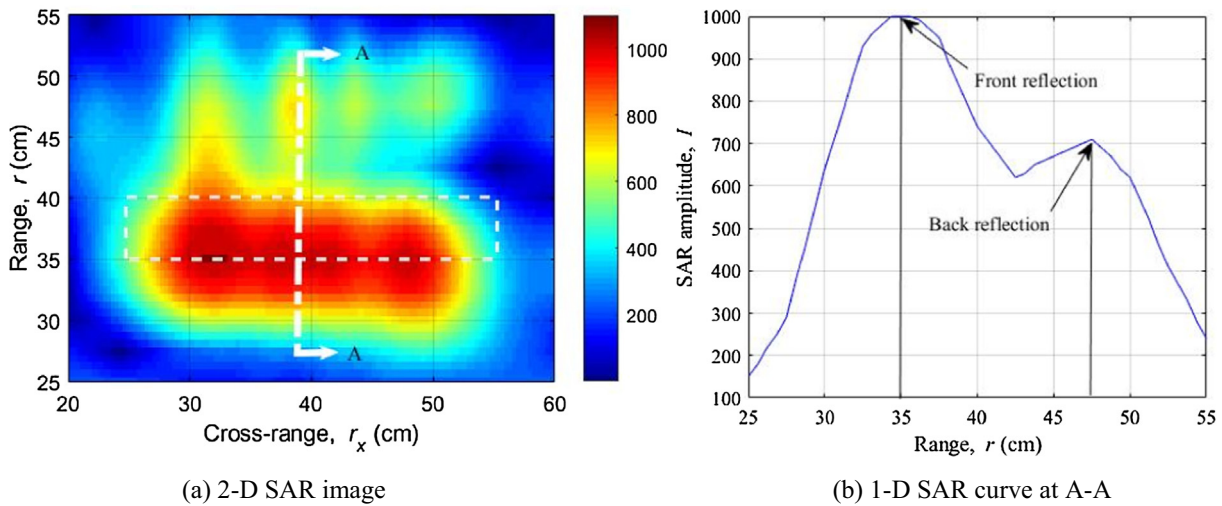

(a) 2-D SAR image

(b) 1-D SAR curve at A-A

Fig. 8. 2-D SAR image and 1-D SAR curve of concrete at $\psi = 0\%$.

(a) 2-D SAR image
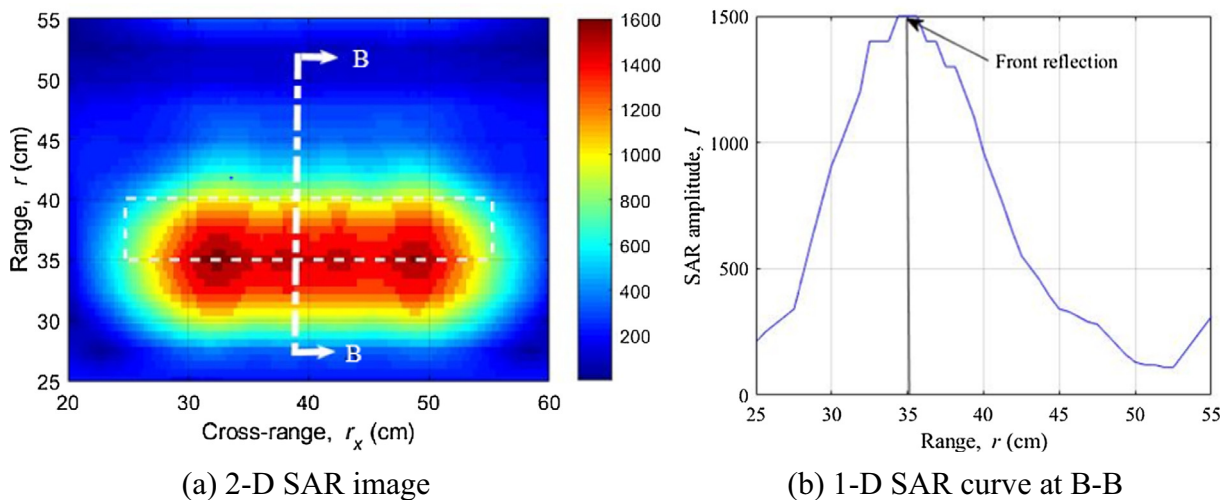
(b) 1-D SAR curve at B-B

Fig. 9. 2-D SAR image and 1-D SAR curve of concrete at $\psi = 3.85\%$.

attenuation. Meanwhile, it is also noteworthy to point out that dielectric amplification of concrete due to moisture can be locally observed by comparing Figs. 8(b) and 9(b) on the SAR amplitude of the first peak.

4.3. SAR image indication of moisture distribution

The 2-D nature of SAR images explicitly suggests their potential for subsurface moisture characterization. As theoretically predicted and experimentally observed in Fig. 5, variation of the moisture level in a concrete panel not only affects SAR amplitudes ($I(r, r_x)$) but also changes in the distribution of SAR amplitudes. Change in the distribution of SAR amplitudes can be related to the change of moisture distribution, in view of the spatial nature of SAR amplitudes. Theoretically, the greater SAR amplitude is, the higher moisture content it has at the location of the SAR amplitude. This is based on the dielectric amplification of concrete due to moisture ingress. In order to use SAR images for referring moisture distribution inside concrete in this research, a critical contour area (A_c) is proposed. In this approach, a contour at representative SAR amplitude is first selected to represent the scattering response of a concrete specimen at given moisture content. The criterion for selecting a representative SAR amplitude is the consistent evolution (expansion and contraction) of moisture distribution. This representative SAR amplitude is chosen such that the moisture level and the moisture distribution inside the concrete panel are positively correlated. In other words, under this assumption, lower moisture contents results in smaller contours in SAR images. For homogeneous materials, this assumption leads to a set of non-overlapped contours representing various moisture contents. Fig. 10 shows the SAR image of the concrete panel at $\psi = 3.85\%$ and its contours at various SAR amplitudes ($I = 400$–1200).

In the SAR imaging result from the concrete panel used in this paper, the specific SAR amplitude was found to be 900 for concrete panels at different moisture levels. Using the specific SAR amplitude, critical contour areas at different moisture levels were obtained from SAR images in Fig. 5, as illustrated in Fig. 11. An empirical model was proposed for the critical contour areas, as shown in Eq. (17).

$$A_c(\psi) = a_3 e^{b_3 \psi} + c_3 \tag{17}$$

where $A_c(\psi)$ = critical contour area at moisture content ψ, ψ = moisture content (%), and a_3, b_3, c_3 = constants ($a_3 = 36.35$, $b_3 = 0.4223$, $c_3 = 82.08$). The R^2 value of the model in Eq. (17) was 0.985. Eq. (17) was inverted to obtain third model of estimating moisture content.

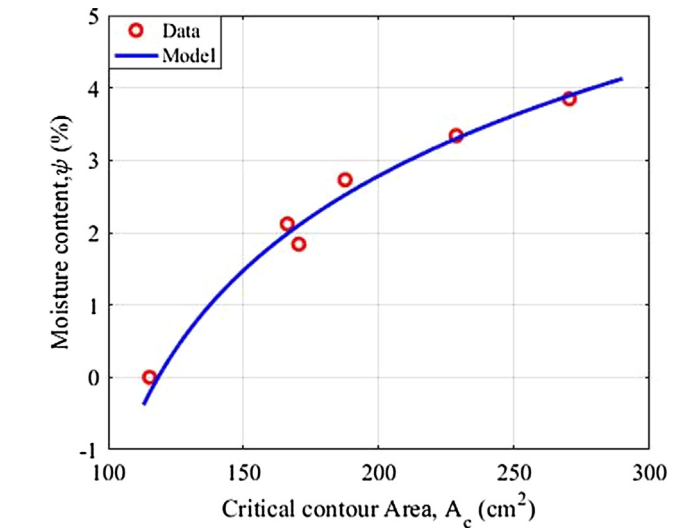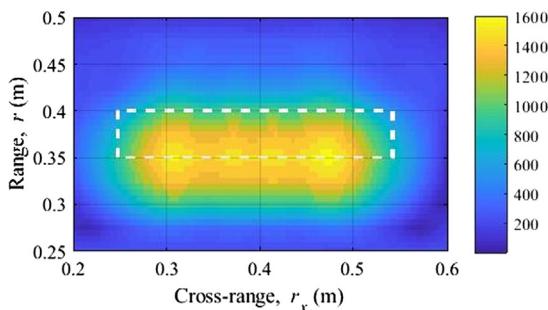$$\psi_{est}(A_c) = \frac{1}{b_3} \log\left(\frac{A_c - c_3}{a_3}\right) \tag{18}$$

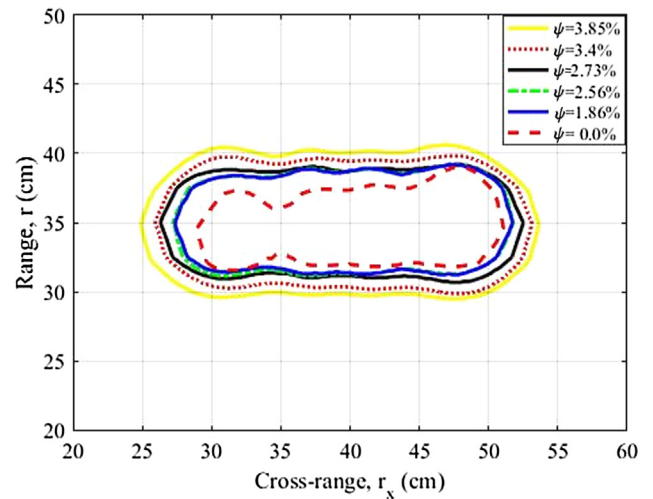**Fig. 11.** Moisture content estimation by using critical area contour (at $I = 900$).

Fig. 12. Critical contours from SAR images representing different moisture contents (at $I = 900$).

where $\psi_{est}(A_c)$ = estimated moisture content (%) using critical contour area A_c. Fig. 12 illustrates the critical contours of SAR images representing different moisture contents at a given SAR amplitude of 900.
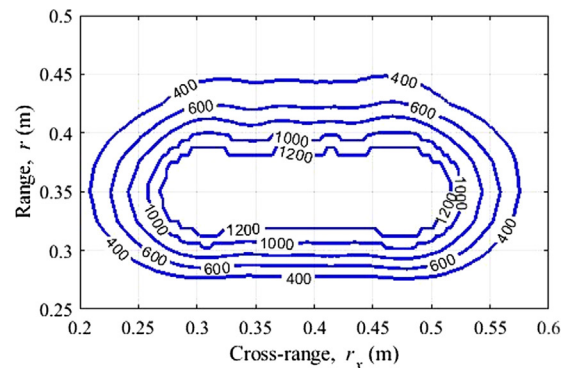

Fig. 10. (a) SAR image at $\psi = 3.85\%$ and (b) its contours at SAR amplitudes $I = 400$–1200.

Table 2
Four models for estimating moisture content inside concrete.

SAR para	Model	Coefficients			R^2
I_{int}	$\psi(I_{int}) = \frac{1}{b_1} \log\left(\frac{I_{int}-c_1}{a_1}\right)$	$a_1 = 1.525\mathrm{e}{+}05$	$b_1 = 0.5585$	$c_1 = 9.303\mathrm{e}{+}05$	0.986
I_{avg}	$\psi(I_{avg}) = \frac{1}{b_{2+}} \log\left(\frac{I_{avg}-c}{a}\right)$	$a_2 = 67.85$	$b_2 = 0.5289$	$c_2 = 692.3$	0.985
A_c	$\psi(A_c) = \frac{1}{b} \log\left(\frac{A_c-c}{a}\right)$	$a_3 = 36.35$	$b_3 = 0.4223$	$c_3 = 82.08$	0.985
$\left(\frac{dI}{dR_A}\right)$	$\psi\left(\frac{dI}{dR_A}\right) = p_1 \frac{dI}{dR_A} + p_2$	$p_1 = 0.003311$	$p_2 = -0.4738.$		0.989

4.4. K-R-I curves of SAR images

In addition to three models in Table 2, another approach applied to analyze SAR images in this paper is the K-R-I transform. The concept of the K-R-I transform is to simultaneously investigate curvature (K), area ratio (R), and amplitude (I) of a SAR image in order to better reveal the features of SAR images. The use of curvature K (average Gaussian curvature) to analyze SAR images is to quantify the shape change of contours. Area ratio R is computed for each contour in order to quantify both specimen size and scattering effect (materials with higher dielectric constants produce greater contours). Amplitude I is used as a reference index to register each set of curvature and area ratio or (K, R). Furthermore, the K-R-I transform eliminates the requirements (e.g., orientation, resolution) in the direct comparison of two SAR images, enabling us to analyze SAR images beyond the limitation of baseline approach for condition assessment. Detail information about the K-R-I transform can be found in [23]. Figs. 13 and 14 show two K-R-I curves and their corresponding SAR images of a concrete panel with two different moisture contents.

While the K-R-I curves in Figs. 13(b) and 14(b) could be quantitatively compared by coefficient of correlation for moisture content difference, the curvature feature of SAR images did not demonstrate distinctive variation from 0.0% moisture content to

3.8% moisture content. This was because the contour shapes of SAR images representing different moisture contents are similar as shown in Fig. 12. In order to develop quantitative models for predicting moisture content of concrete, R-I curves of SAR images were used for modeling. Fig. 15 compares R-I curves of SAR images representing a concrete panel with different moisture contents from 0% to 3.85%.

In Fig. 15, it was found that the slope of R-I curves of a SAR image representing higher moisture contents is greater than the one of R-I curves of a SAR image representing lower moisture contents. This pattern held true for all moisture contents except for ψ = 1.84%. Slopes of R-I curves in Fig. 15 were calculated, as shown in Fig. 16. The moisture content prediction model using the slope of R-I curves was proposed in Eq. (19).

$$\psi_{est}\left(\frac{dI}{dR_A}\right) = p_1 \frac{dI}{dR_A} + p_2 \tag{19}$$

where $\psi_{est}\left(\frac{dI}{dR_A}\right)$ = estimated moisture content (%), $\frac{dI}{dR_A}$ = slope of R-I curves at different moisture contents, $p_1 = 0.003311$, and $p_2 = -0.4738$. The R^2 of the model (Eq. (19)) was 0.989.

In Fig. 16, it was found that the slopes of R-I curves representing moisture contents 2.12%, 2.73%, 3.4% and 3.85% follow a linear
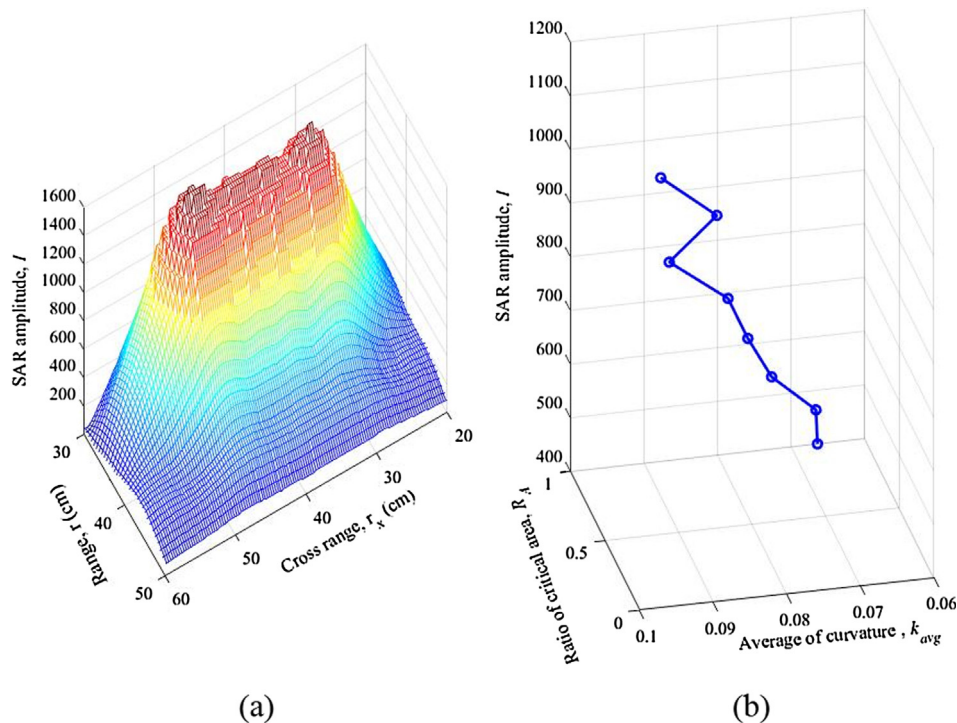

(a)   (b)

Fig. 13. K-R-I curve of a SAR image of concrete – moisture content ψ = 3.85%.
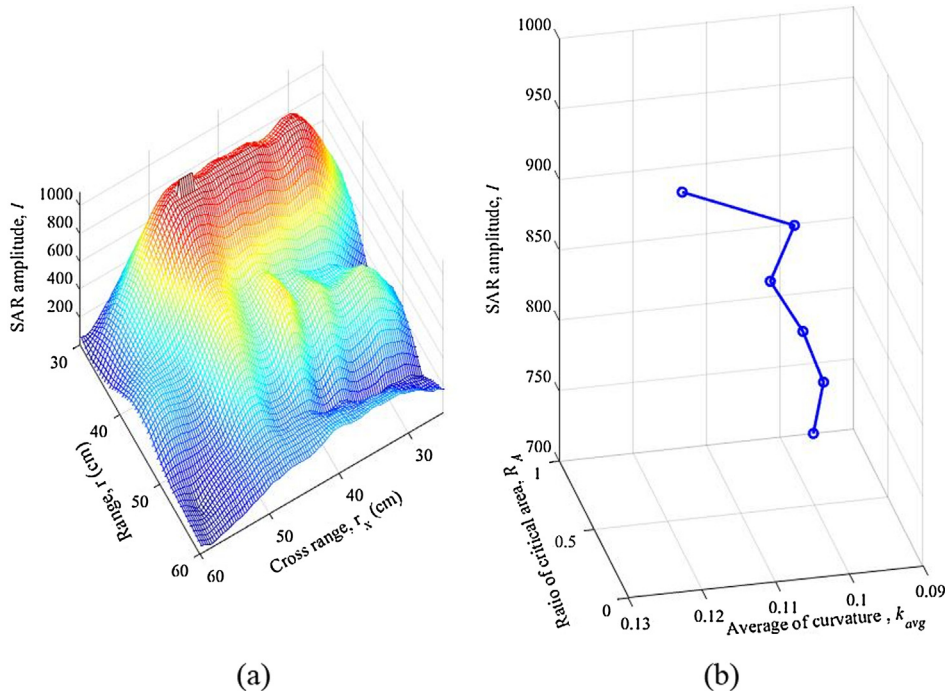
(a)

(b)

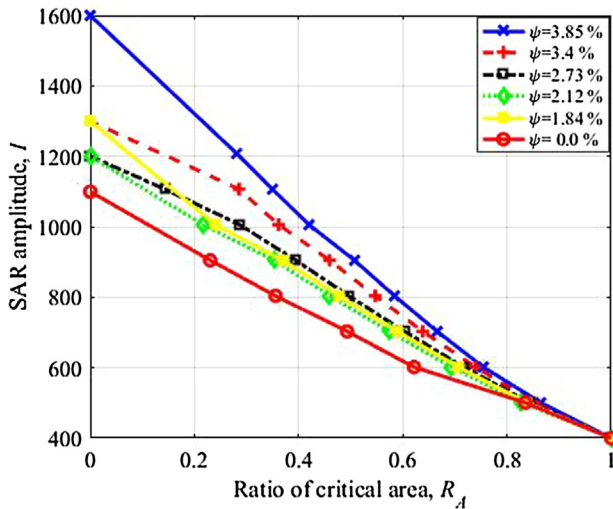**Fig. 14.** K-R-I curve of a SAR image of concrete – moisture content ψ = 0%.

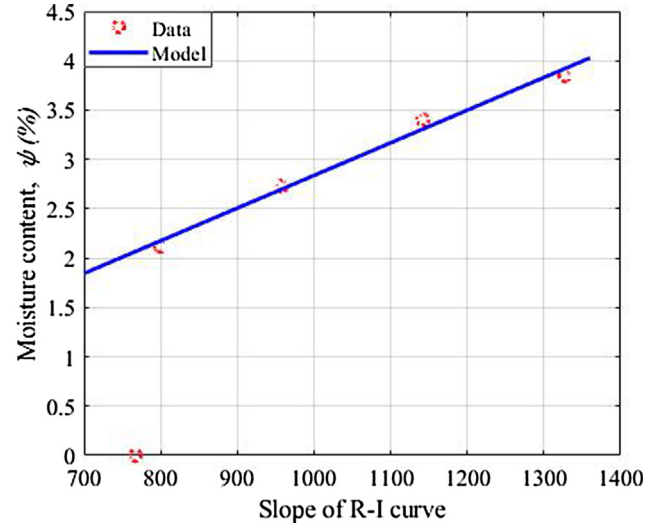**Fig. 15.** R-I curves of SAR images – ψ = 0%–3.85%

Fig. 16. Slopes of R-I curves representing different moisture contents (ψ = 0%–3.85%).

pattern, except the one of 0% moisture content. This was because the 0% moisture content of concrete was achieved by oven-heating, while all other moisture contents were achieved by air-drying. The oven-heated state (ψ = 0%) of the concrete panel was created by introducing an internal high pore pressure (due to thermal expansion) inside concrete, in which the rheological profile of some gel pores (micropores) and capillary pores (large mesopores) has been changed. On the other hand, air-drying of the concrete panel was driven by moisture diffusion in which the rheological profile of all pores (gel and capillary) remains unchanged. This difference explained why the oven-heating point does not follow the trend of other air-drying points in Fig. 16. Eq. (19) represents the fourth model for moisture content estimation of concrete. All three models for estimating moisture content are summarized in Table 2.

5. Conclusion

This paper presents an approach to quantitatively analyze SAR images of concrete for moisture characterization, by investigating the use of SAR (synthetic aperture radar) imaging for moisture content inside a concrete panel specimen. A 10.5 GHz continuous wave imaging radar system with 1.5 GHz bandwidth was applied in this research. The SAR images generated in stripmap imaging mode from a concrete panel with moisture content ranging from 0% to 3.85% were used in developing quantitative models for internal moisture characterization. Major research findings are concluded in the following.

- Moisture content – From our experimental imaging result, linear increase of moisture content inside a concrete panel can result in a nonlinear increase of SAR amplitudes (integrated SAR amplitude I_{int} and average maximum SAR amplitude I_{avg}), as shown in Figs. 6 and 7. Furthermore, the increase of moisture content in concrete also results in the amplification of dielectric properties of concrete. This was experimentally found in Figs. 8 and 9. In Figs. 8 and 9, the increase of first peak SAR amplitude indicates the increase of dielectric constant of concrete, while the decrease of second peak SAR amplitude suggests the increase of loss factor of concrete. Four quantitative models are developed from the SAR images of a concrete panel specimen in this research.

- Moisture distribution – Our experimental imaging result indicates that variation of the moisture level inside a concrete panel not only affects SAR amplitudes ($I(r, r_x)$) but also changes in the distribution of SAR amplitudes (Fig. 12). A critical contour area approach is proposed not only for estimating moisture content but also for inferring moisture distribution.

Conflict of interest

None.

References

[1] Z. Wang, Q. Zeng, L. Wang, Y. Yao, K. Li, Effect of moisture content on freeze–thaw behavior of cement paste by electrical resistance measurements, J. Mater. Sci. 49 (12) (2014) 4305–4314.

[2] Q. Zeng, T. Fen-Chong, P. Dangla, K. Li, A study of freezing behavior of cementitious materials by poromechanical approach, Int. J. Solids Struct. 48 (22) (2011) 3267–3273.

[3] H. Cai, X. Liu, Freeze-thaw durability of concrete: ice formation process in pores, Cem. Concr. Res. 28 (9) (1998) 1281–1287.

[4] A. Bentur, S. Diamond, N.S. Berke, Steel Corrosion in Concrete, E and FN Spon, London, 1997.

[5] D. Russell, P.M. Basheer, G.B. Rankin, A.L. Long, Effect of relative humidity and air permeability on prediction of the rate of carbonation of concrete, Proc. Inst. Civ. Eng. Struct. Build. 146 (3) (2001) 319–326.

[6] A. Carles-Gibergues, M. Cyr, Interpretation of expansion curves of concrete subjected to accelerated alkali–aggregate reaction (AAR) tests, Cem. Concr. Res. 32 (5) (2002) 691–700.

[7] G. Fagerlund, The critical degree of saturation method of assessing the freeze/thaw resistance of concrete, Mater. Struct. 10 (4) (1977) 217–229.

[8] J.A. Gonzalez, W. Lopez, P. Rodriguez, Effects of moisture availability on corrosion kinetics of steel embedded in concrete, Corrosion 49 (12) (1993) 1004–1010.

[9] D. Stark, The moisture condition of field concrete exhibiting alkali-silica reactivity, in: CANMET/ACI Second International Conference on Durability of Concrete, SP-126, American Concrete Institute, Farmington Hills, Michigan, 1991, pp. 973–987.

[10] S.N. Shoukry, G.W. William, B. Downie, M.Y. Riad, Effect of moisture and temperature on the mechanical properties of concrete, Constr. Build. Mater. 25 (2) (2011) 688–696.

[11] D. Chen, A. Wimsatt, Inspection and condition assessment using ground penetrating radar, J. Geotech. Environ. Eng. 136 (1) (2010) 207–214.

[12] H. Akita, T. Fujiwara, Y. Ozaka, A practical procedure for the analysis of moisture transfer within concrete due to drying, Mag. Concr. Res. 49 (179) (1997) 129–137.

[13] J. Šelih, C.S. Antonio, W.B. Theodore, Moisture transport in initially fully saturated concrete during drying, Transp. Porous Media 24 (1) (1996) 81–106.

[14] S. Multon, E. Merliot, M. Joly, F. Toutlemonde, Water distribution in beams damaged by Alkali-Silica Reaction: global weighing and local gammadensitometry, Mater. Struct. 37 (2004) 282–288.

[15] G. Villain, M. Thiery, Gammadensimetry: a method to determine drying and carbonation profiles in concrete, Nondestruct. Test. Eva. (NDT & E) Int. 39 (4) (2006) 328–337.

[16] BlueRock by Giatec, Inc., BlueRock™ | Concrete Humidity Sensor. https://www.giatecscientific.com/concrete-sensors/bluerock/, 2018 (accessed 29 January 2018).

[17] Z.M. Sbartai, S. Laurens, J.P. Balayssac, G. Ballivy, G. Arliguie, Effect of concrete moisture on radar signal amplitude, ACI Mater. J. 103 (6) (2006) 419.

[18] Z.M. Sbartai, S. Laurens, J.P. Balayssac, G. Ballivy, G. Arliguie, Using radar direct wave for concrete condition assessment: correlation with electrical resistivity, J. Appl. Geophys. 62 (4) (2007) 361–374.

[19] J.B. Cornell, A.T. Coote, The application of an infrared absorption technique to the measurement of moisture content of building materials, J. Appl. Chem. Biotechnol. 22 (4) (1972) 455–463.

[20] G. Quincot, M. Azenha, J. Barros, R. Faria, State of the art–Methods to measure moisture in concrete, Projetos De InvestigaçãoCientífica E DesenvolvimentoTecnológico, Portugal, 2011.

[21] S.F. Senin, R. Hamid, Ground penetrating radar wave attenuation models for estimation of moisture and chloride content in concrete slab, Constr. Build. Mater. 106 (2016) 659–669.

[22] T.Y. Yu, Distant damage-assessment method for multilayer composite systems using electromagnetic waves, J. Eng. Mech. 137 (8) (2011) 547–560.

[23] T.Y. Yu, Quantitative assessment of CFRP-concrete Cylinders using synthetic aperture radar images, Res. Nondestr. Eval. 28 (3) (2017) 168–185.

[24] S. Laurens, J.P. Balayssac, J. Rhazi, G. Arliguie, Non-destructive evaluation of concrete moisture by GPR: experimental study and direct modeling, Mater. Struct. 38 (2005) 827–832.

[25] G. Klysz, J.P. Balayssac, Determination of volumetric water content of concrete using ground-penetrating radar, Cem. Concr. Res. 37 (2007) 1164–1171.

[26] S. Laurens, J.P. Balayssac, J. Rhazi, G. Arliguie, Influence of concrete relative humidity on the amplitude of Ground-Penetrating Radar (GPR) signal, Mater. Struct. 35 (4) (2002) 198–203.

[27] Z.M. Sbartaï, S. Laurens, D. Breysse, Concrete moisture assessment using radar NDT technique–comparison between time and frequency domain analysis, Non-Destructive Testing in Civil Engineering (NDTCE'09), Nantes, France, 2009.

[28] J.A. Kong, Electromagnetic Wave Theory, EMW Publishing Cambridge, MA, 2000.

[29] L. Tsang, J.A. Kong, K.H. Ding, Scattering of Electromagnetic Waves—Theories and Applications, Wiley, New York, 2000.